nature communications

Article

https://doi.org/10.1038/s41467-026-73328-1

Local polarity modulation in triangular pores of covalent organic frameworks for iodine capture from water

Received: 28 October 2025

Accepted: 9 May 2026

Published online: 20 May 2026

Check for updates

Mengjie Hao[1], You Wu[1], Juyao Zhang[1], Xiaolu Liu[1,2], Juncheng Liang[2], Ming Lei[1], Xinyue Zhang[1], Zhongshan Chen[1], Hui Yang[1] ✉, Geoffrey I. N. Waterhouse[3], Abdullah M. Al-Enizi[4], Ayman Nafady[4], Shengqian Ma[5] ✉ & Xiangke Wang[1] ✉

Radioactive iodine from nuclear fission processes can enter water systems in various ways, adversely affecting human health and the environment. Herein, we construct a series of covalent organic frameworks (COFs) with triangular pores and different local polarities for efficient iodine ($I_2 + I^- \rightleftharpoons I_3^-$) capture from aqueous solution. Triangular pores containing weakly polar units show a strong affinity for nonpolar iodine via hydrophobic interactions, whilst the periodically ordered frameworks and intrinsic interlayers based on aromatic moieties and nitrogen-containing groups capture I_2 and I_3^- through van der Waals forces and charge transfer. COF-1 with weak local polarity delivers a high iodine (^{131}I) adsorption capacity, fast adsorption kinetics, and excellent selectivity in tap water, groundwater, and seawater. Moreover, COF-1 exhibits an exceptional trace iodine removal efficiency (from ~200 ppb to below ~65.9 ppb in tap water and ~58.3 ppb in groundwater), making it a promising adsorbent for efficiently treating aqueous iodine waste streams.

Radioactive iodine is generated as a waste product in nuclear fission reactors and nuclear medicine departments in hospitals, and eventually some of the iodine flows in aqueous form into wastewater-treatment facilities[1–3]. The growth of nuclear waste streams containing a large amount of ^{131}I and ^{129}I as volatile radioactive pollutants has underscored the critical importance of nuclear waste management[4,5]. Once an accident occurs, radioactive iodine will be released into the environment. The Fukushima nuclear accident led to the release of 8.06 GBq (1.2 kg) ^{129}I and 1.5×10^7 kg ^{131}I[6–8]. At radiological waste disposal sites, such as the Hanford Site and the Savannah River Site, ^{129}I poses a risk due to the high inventory and high mobility of iodine species[9]. These scenarios potentially allow radioactive iodine to enter groundwater, seawater and tap water through nuclear accidents or nuclear waste management operations[10,11]. Removing iodine from the source and contaminated aquatic systems to reduce the radioactivity and volume of wastewater is an important step in pollution control[12]. ^{129}I is a long-lived beta-emitter with a half-life of ~1.6×10^7 years, whilst ^{131}I is a short-lived beta-emitter that poses a much great threat to human health and the environment[13]. Radioactive iodine is highly soluble in water, existing as molecular iodine (I_2) or triiodide (I_3^-). For this reason, it presents a serious health risk to humans via contaminated drinking water or foods[14,15]. Ingestion of radioactive iodine can cause hypothyroidism, malformed fetuses, and thyroid cancer[16,17]. Mitigating the potential impacts of radioactive iodine contamination and meeting the need for rapid response to nuclear accidents have motivated the search for adsorbents with fast kinetics, high adsorption capacity, and strong selectivity for capturing aqueous iodine species.

[1]College of Environmental Science and Engineering, North China Electric Power University, Beijing, P.R. China. [2]Division of Ionizing Radiation, National Institute of Metrology, Beijing, PR China. [3]School of Chemical Sciences, The University of Auckland, Auckland, New Zealand. [4]Department of Chemistry, College of Science, King Saud University, Riyadh, Saudi Arabia. [5]Department of Chemistry, University of North Texas, Denton, TX, USA.
✉e-mail: h.yang@ncepu.edu.cn; shengqian.ma@unt.edu; xkwang@ncepu.edu.cn

A myriad of strategies have been pursued for the capture of iodine from water[18–20]. For many adsorbents, iodine capture is hampered by interference of water molecules, competing ions and pH, resulting in unsatisfactory iodine uptake capacities and slow kinetics[21–27]. For example, traditional porous adsorbents, including activated carbon, aerogels, silica, and silver-doped zeolites, have all been applied for the capture of iodine[28–31]. However, these materials suffer from limitations, such as low capture capacities, slow adsorption rates, and poor selectivity, inter alia in water[32]. Accordingly, researchers are now pursuing porous frameworks as tailorable adsorbents for high-performance iodine capture. Notably, metal-organic frameworks (MOFs), covalent organic frameworks (COFs), and porous organic cages (POCs) are increasingly being applied for iodine adsorption[33–38]. These intrinsically porous materials offer distinct advantages over traditional adsorbents, such as rapid adsorption kinetics, high adsorption capacities, and good selectivity. For such adsorbents, achieving a high iodine capture capacity has relied on the synergistic effect of multiple nitrogen-containing functional groups to create active sites (Fig. 1a). For example, N-MOF-PAN fibers were prepared containing different nitrogen-containing building units, such as cationic quaternary ammonium, amine, and UiO-66-NH_2. Owing to synergies involving the different N groups, 94.6% removal of I_2 was achieved from a saturated solution within 180 min and 98.7% of iodine from a I_3^- solution within 240 min[39]. A similar hybridization synthetic strategy was utilized to synthesize a composite crystalline aerogel material, composed of amino-functionalized metal-organic polyhedra and imine-functionalized covalent organic framework[40]. The composite demonstrated a high aqueous iodine (I_2 and I_3^-) adsorption capacity, fast adsorption kinetics, and reusability. Further, the composite showed high selectivity for I_3^- compared to other anions like NO_3^-, Cl^-, SO_4^{2-}, Br^-, etc. Furthermore, channel surfaces that support diverse functional groups can also tune affinity for iodine. COFs as crystalline porous materials can be designed with different topologies, well-defined π skeletons and tunable pore sizes, making them suitable for selective capture of neutral I_2[41–48]. Ke and co-workers designed crystalline HcOF-1, with the hydrophobic nature of the pores enabling efficient iodine capture (adsorbing 2.1 g/g of iodine from KI/I_2 aqueous solution)[49]. Ma et al. synthesized COFs with an optimized local chemical environment of iodine-binding N-sites, and the COFs can remove 99.5% aqueous I_2 and I_3^- from high-salinity aqueous environments[50]. The key to achieving effective capture in porous adsorbent materials lies in providing a strong affinity and accessible channels for iodine. However, the ideal pore characteristics of frameworks required for effective iodine capture in water are not yet well understood, motivating further research.

Herein, a strategy for regulating the local polarity in triangular pores of COFs is proposed, elaborated to generate extended crystalline frameworks with triangular topology and fine-tuned local polarity for optimal iodine adsorption (Fig. 1b). Leveraging the nonpolar structural characteristics of I_2 and I_3^-, wherein the charge is uniformly distributed across each iodine atom, we designed a series of COFs with tailored frameworks. Firstly, hexavalent 4,4′,4″,4‴,4⁗,4⁗′-(triphenylene-2,3,6,7,10,11-hexayl)hexabenzaldehyde (HFPTP) nodes are connected to linear 4,4″-diamino-p-terphenyl (DPT) linkers through imine bonds, creating COF-1. Subsequently, a 4,4′-(1H-benzo[d]imidazole-4,7-diyl)dianiline (DBID) was used as a substitute for DPT to obtain COF-2, containing imidazole units in the framework. Finally, 2,3,8,9,14,15-hexa(4-formylphenyl)diquinoxalino [2,3-a:2′,3′-c]phenazine (HATN) was introduced into the COF-3 by the replacement of HFPTP, aggregating imidazole and phenazine units. The structural design approach, involving tuning the node and linker to control nitrogen-containing units and local polarities in the triangular pores of the COFs, was then scrutinized for aqueous iodine capture. The weakly polar framework (COF-1) exhibited an excellent iodine adsorption capacity in water (2.01 g/g in I_2 solution and 7.12 g/g in a KI/I_2 solution), higher than COF-2 and COF-3 with stronger local polarity. COF-1 achieved efficient and rapid iodine removal in different types of water (tap water, groundwater and seawater), worked over a wide pH range (from 1 to 9), and showed good selectivity in the presence of a large excess of competing anions (NO_3^-, HCO_3^-, Cl^-, SO_4^{2-}, and CH_3COO^-). In addition, COF-1 can rapidly remove iodine (I_2 or I_3^-) from dilute contaminated mixed solutions, tap water and groundwater. Starting at an initial concentration of ~200 ppb, COF-1 quickly lowered the iodine concentrations to 22.8 ppb (for an I_2 solution), 27.3 ppb (for a I_3^- solution), 65.9 ppb (for I_3^- in tap water) and 58.3 ppb (for I_3^- in groundwater). Mechanism studies revealed that the periodic triangular pore channels in COF-1 provide high porosity and a regular interlayer to adsorb iodine by π-conjugation interactions. The weakly polar pore environment derived from aromatic units together with nitrogen-containing groups (imine bonds) effectively captures structurally nonpolar I_2 and I_3^- via hydrophobic interactions, charge transfer, and van der Waals forces (Fig. 1c). This study offers new vistas for designing adsorbent materials for the capture of structurally nonpolar iodine and other pollutants from water, with the findings being useful for both environmental remediation and water purification.

Results

Synthesis and structure characterizations

To deconvolute the relationships between the structural properties of COFs and their performance for iodine capture in water, we adopted a local polarity regulation strategy by fabricating different nitrogen-containing C_6 nodes and C_2 linkers (Fig. 1b). As shown in Fig. 2a, highly crystalline COF-1 was synthesized by the condensation of HFPTP with DPT under optimized solvothermal conditions using 6 M AcOH as the catalyst and heating at 120 °C for 3 days. The structure of COF-1 was examined via element analysis (EA), Fourier-transformed infrared (FT-IR) spectroscopy, ^{13}C solid-state CP/MAS NMR spectroscopy, and powder X-ray diffraction (PXRD). The EA result (found: C 84.47%, N 5.44%, H 6.52%) showed close agreement with theoretical values (C 89.76%, N 5.51%, H 4.72%), with minor deviations plausibly arising from trapped solvent molecules (Supplementary Table 1). In the FT-IR spectra, a new C = N stretching mode appeared at 1624 cm^{-1}, at the expense of the C = O stretching mode and $-NH_2$ signal in the starting materials, which indicated successful aldehyde-amine condensation reactions (Fig. 2b)[51]. The ^{13}C solid-state CP/MAS NMR spectrum of COF-1 showed the characteristic peak of imine moieties at ~158 ppm, further confirming the formation of imine bonds (Fig. 2c)[46]. COF-1 showed PXRD peaks at 3.0, 5.1, 5.9, 7.8, and 8.9°, which could readily be assigned to (100), (110), (200), (210), and (300) crystal facets, respectively (Fig. 2d). Pawley refinement revealed that COF-1 possessed an eclipsed AA stacking model, consistent with the experimental data. COF-1 crystallized in the P1 space group, with lattice parameters of a = 34.42 Å, b = 34.42 Å, c = 3.75 Å, and α = 80.62°, β = 84.20°, and γ = 120.02° (R_{wp} = 5.63%, R_p = 3.87%) (Supplementary Table 2). The theoretical structure of COF-1 showed triangular 1D open channels of size 1.3 and 1.6 nm, with the π-π stacking distance between individual layers estimated to be ~3.75 Å (Fig. 2e). To further investigate the intrinsic porosity of COF-1, N_2 adsorption-desorption isotherms were measured at 77 K (Fig. 2f). The Brunauer-Emmett-Teller (BET) surface area of COF-1 was calculated to be 406.2 m^2/g. COF-1 showed a typical type-I isotherm, indicating that abundant micropores were present in the COF-1. Figure 2f (inset) shows that the pore size distribution derived from the nonlocal density functional theory (NLDFT) method was predominantly centered at 1.2-1.6 nm, good accord with the channel sizes predicted by simulation. Scanning electron microscopy (SEM) images showed COF-1 retained layered morphology (Supplementary Fig. 1). Lattice fringes with a spacing of 1.8 nm were observed from the transmission electron microscopy (TEM) image of COF-1, corresponding to the 1D channels in the AA stacking frameworks (Fig. 2g). And COF-1 exhibited lattice fringes with

https://doi.org/10.1038/s41467-026-73328-1

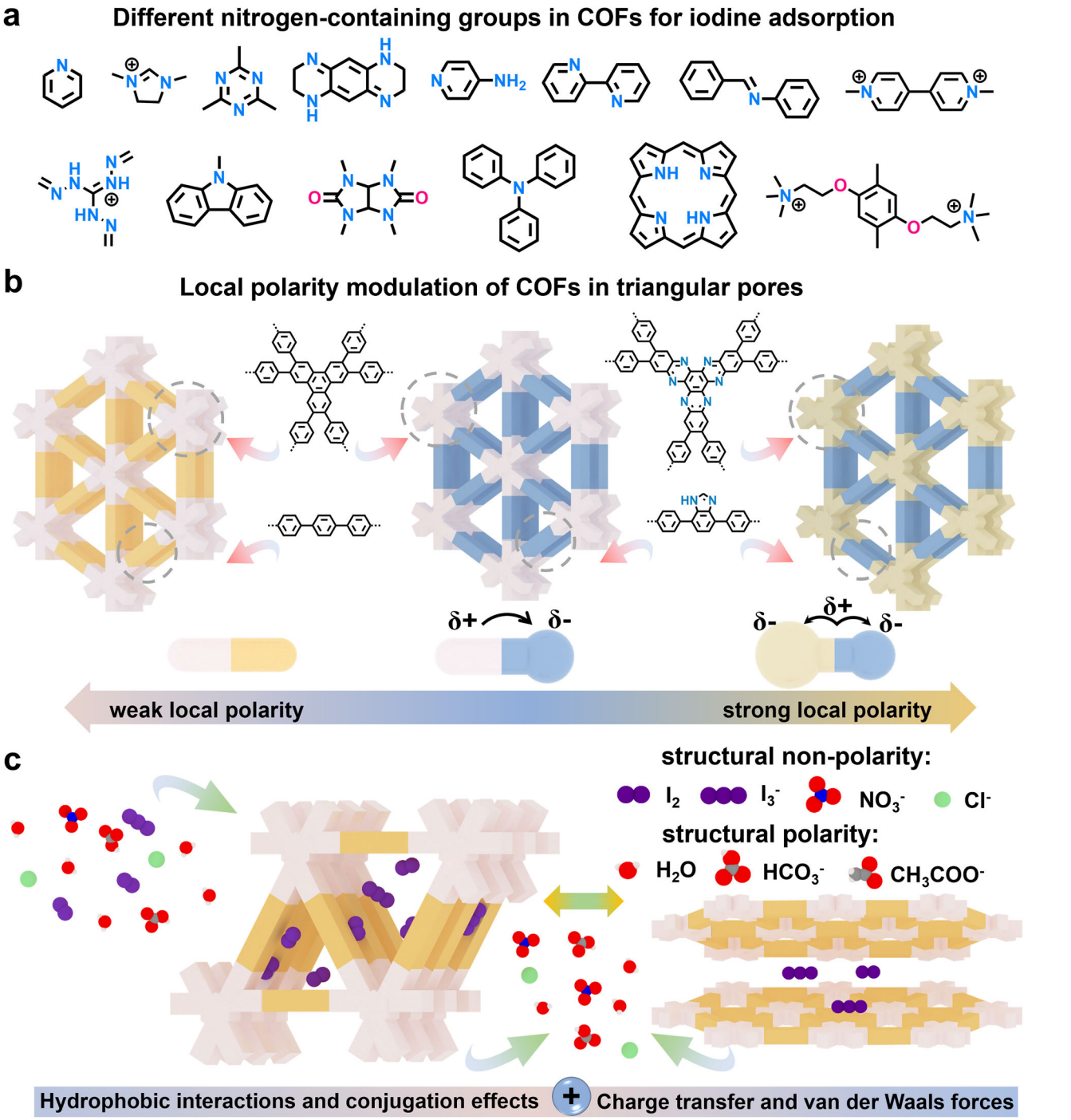


Fig. 1 | Schematic illustration of a local polarity modulation strategy in triangular pores of COFs for iodine adsorption. a Common iodine adsorption sites in COF materials containing abundant nitrogen-containing groups. **b** Schematic illustration of the different local polarities of COFs regulated by different nitrogen-containing building units. **c** Illustration of triangular COFs with weak local polarity providing available pores and structural layers for nonpolar iodine adsorption, highlighting efficient iodine capture programmed by the combination of hydrophobic interactions, charge transfer, van der Waals forces, and conjugation effects.

a spacing of 3.6 Å, which is attributed to the interlayer stacking distance (Supplementary Fig. 2). Water contact angle measurements were used to determine the surface properties of the COFs, with the contact angle of COF-1 determined to be 126.3° (Fig. 2h). The characterization data unequivocally confirmed the successful synthesis of COF-1.

Next, geometrically similar monomers were adopted as adjustable modules, with different N-heterocycles used to regulate the local polarity of COFs precisely. COF-2 was obtained by substituting DPT in COF-1 for DBID, and COF-3 was obtained by substituting HFPTP and DPT for HATN and DBID, respectively, thereby introducing imidazole units and phenazine units into their frameworks (Fig. 3a). EA results revealed that the compositions of both COF-2 and COF-3 closely matched their theoretical values, confirming the successful preparation of the targeted frameworks (Supplementary Table 1). FT-IR spectra of COF-2 and COF-3 displayed the characteristic imine C = N stretching vibration at 1624 cm^{-1}, along with C – N bond vibrations at 1354 cm^{-1} due to N-containing modules in both COFs (Fig. 3b). ^{13}C CP/MAS NMR spectra revealed the signals of C – N moieties in the imidazole and phenazine groups of COF-2 and COF-3 at 135 and 142 ppm, respectively (Fig. 3c). The characteristic peak at 158 ppm was due to

https://doi.org/10.1038/s41467-026-73328-1

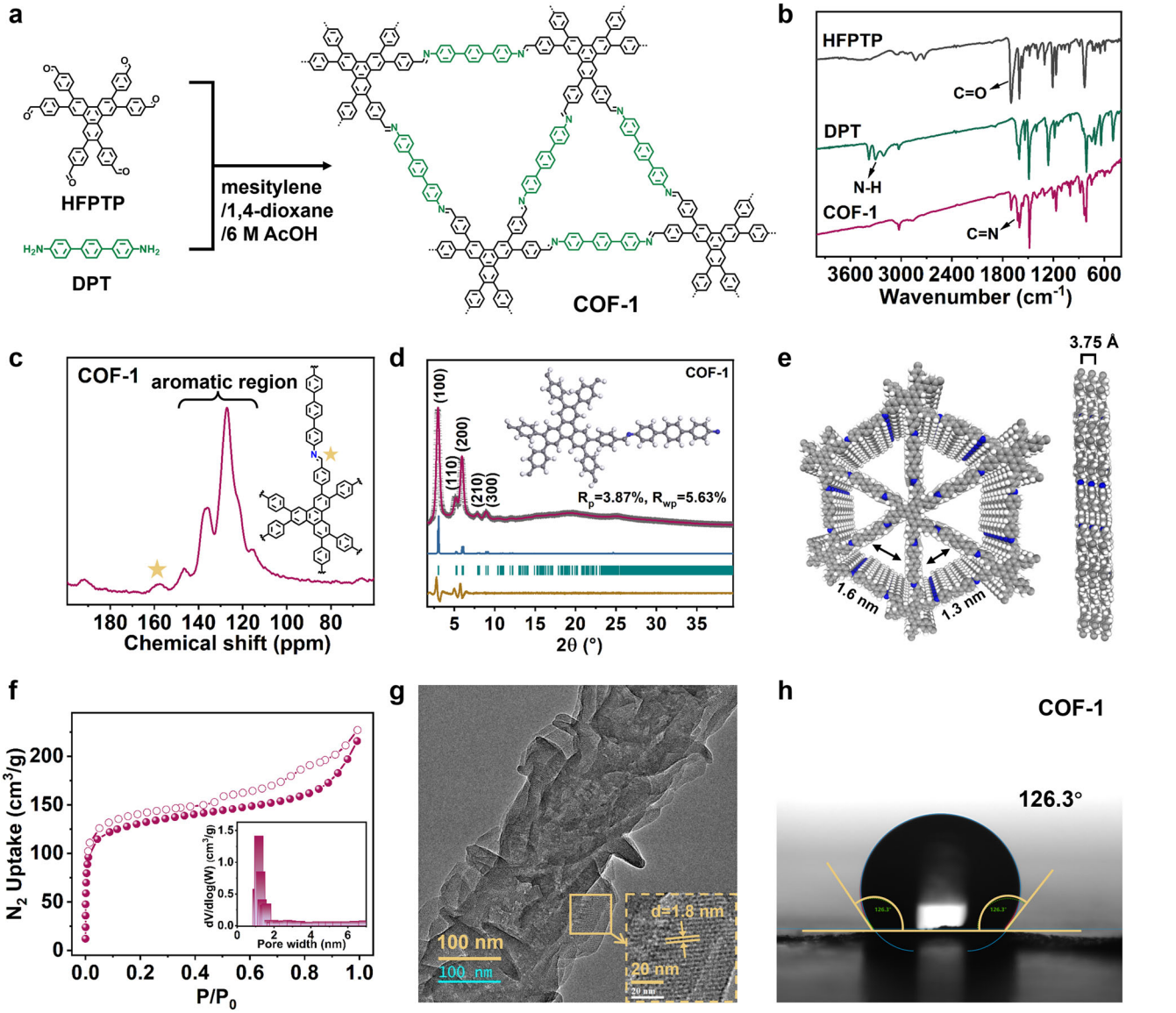


Fig. 2 | Chemical structure and characterization of COF-1. a Illustration of the synthesis of COF-1. **b** FT-IR spectra of COF-1 and linkers. **c** ^{13}C solid-state CP/MAS NMR spectrum of COF-1. **d** Experimental PXRD pattern of COF-1 with corresponding Pawley refinement (pink), simulated results (blue), and Bragg positions (turquoise) showing good fits to the experimental data (gray) with minimal differences (khaki). **e** Top and side views of eclipsed AA stacking in COF-1. The C, N, and H atoms are represented by gray, blue and white spheres, respectively. **f** N_2 adsorption-desorption isotherm and pore size distribution (inset) measured at 77 K for COF-1. **g** TEM image of COF-1 (inset: expanded view showing the lattice spacing). **h** Contact angle for deionized water on a pressed pellet of COF-1.

imine bonds. PXRD analyses and theoretical structural simulations revealed the crystalline structures of as-synthesized COF-2 and COF-3. COF-2 exhibited distinct peaks at 2θ = 3.0° and 6.0°, corresponding to (010) and (020) planes, respectively (Fig. 3d). A triclinic crystal model and Pawley refinement of COF-2 provide a good agreement factor (R_{wp} = 1.96%, R_p = 1.54%) (Supplementary Table 3). The theoretical pore diameters of COF-2 were ~0.8 and 1.1 nm (Supplementary Fig. 3). COF-3 with a bigger unit cell had diffraction peaks shifted towards lower diffraction angles[52], with peaks at 2θ = 2.9° and 5.5° readily assigned to (100) and (020) planes, respectively (Fig. 3e). The experimental data agreed with an eclipsed AA stacking mode for COF-3 belonging to the space group P1, with unit cell parameters (a = 38.43 Å, b = 37.66 Å, c = 3.83 Å, α = 101.60°, β = 84.63°, and γ = 119.58°, R_{wp} = 2.77%, R_p = 2.23%) (Supplementary Table 4). COF-3 possessed a 2D crystal structure with the theoretical channels of size 1.1 and 1.5 nm (Supplementary Fig. 4). Furthermore, the N_2 adsorption-desorption curves showed type-I behavior with pore size distributions of COF-2 and COF-3 concentrated around 0.8-1.2 nm and 1.2-1.6 nm, respectively (Supplementary Figs. 5, 6). These pore sizes closely matched the simulated models, verifying the structural accuracy of both COFs. COF-2 and COF-3 exhibited the BET surface areas of 334.7 and 297.2 m^2/g, respectively. SEM images showed that COF-2 and COF-3 possess aggregated nanoparticle morphologies (Supplementary Fig. 7). COF-2 and COF-3 displayed water contact angles of 110.0° and 4.5°, respectively (Fig. 3f). Compared to COF-1, the increase in nitrogen units enhanced hydrophilicity, which is related to strong local polarity. In particular, COF-3 with a nitrogen-rich framework exhibited high hydrophilicity.

Good stability is a prerequisite for the practical application of COFs in radioactive iodine capture and other applications. Thus, we explored the thermal and irradiated stability of each COF under different conditions. Thermogravimetric analysis (TGA) under a N_2 atmosphere revealed that COF-1 possessed high thermal stability, with almost no weight loss observed below 450 °C (Supplementary Fig. 8).

https://doi.org/10.1038/s41467-026-73328-1

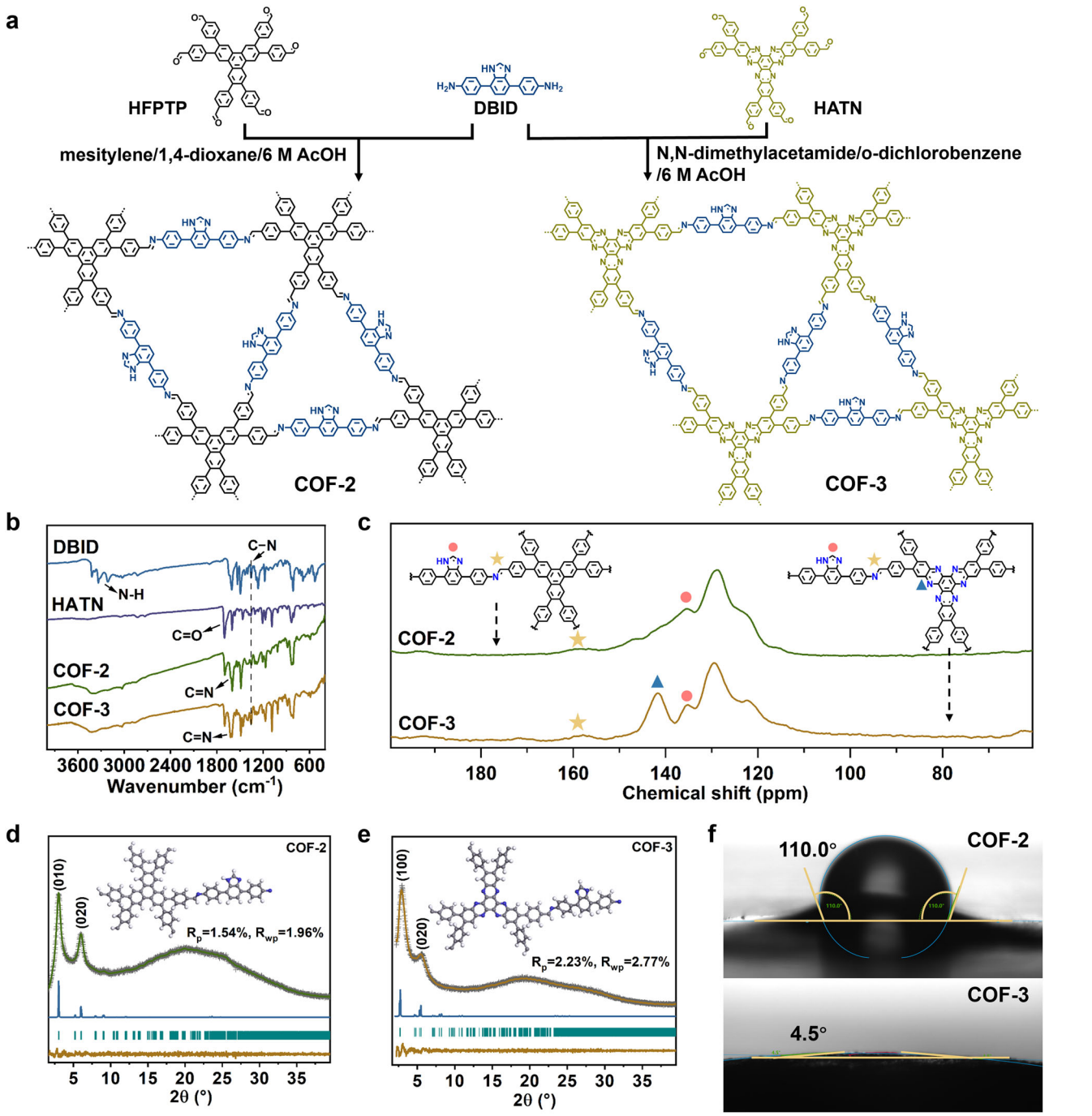


Fig. 3 | Chemical structure and characterization of COF-2 and COF-3. **a** Illustration of the synthesis of COF-2 and COF-3. **b** FT-IR spectra of COF-2, COF-3, and linkers. **c** ^{13}C solid-state CP/MAS NMR spectra of COF-2 and COF-3. **d**,**e** Experimental PXRD patterns of COF-2 and COF-3 with corresponding Pawley refinement (green or yellow), simulated results (blue), and Bragg positions (turquoise) showing good fits to the experimental data (gray) with minimal differences (khaki). **f** Contact angles for deionized water on pressed pellets of COF-2 and COF-3.

TGA profiles of COF-2 and COF-3 showed a small weight loss below 150 °C due to desorption of adsorbed solvent molecules, then showing good stability up to ~620 °C. Radiation tolerance is crucial for radionuclide extraction. Thus, the COFs were subjected to 200 kGy γ-ray exposure. PXRD patterns and FT-IR spectra confirmed the integrity of the frameworks and the retention of important functional groups after the radiation treatment, suggesting that COFs had acceptable radiation stability (Supplementary Fig. 9). After treatment in different pH solutions, COF-1 retained the original PXRD profile, revealing the good chemical stability (Supplementary Fig. 10).

These comprehensive structural characterization studies on COF-1, COF-2, and COF-3 provide a solid foundation for exploring polarity effects in triangular pores on iodine adsorption. The specific COF structures, with different local polarity, were expected to cover structurally nonpolar I_2 and I_3^- capture.

Iodine Adsorption Performance

Aqueous radioactive iodine wastes are produced by nuclear fission reactors. In addition, nuclear accidents can cause contamination of tap water, groundwater and the ocean, creating various types of

https://doi.org/10.1038/s41467-026-73328-1

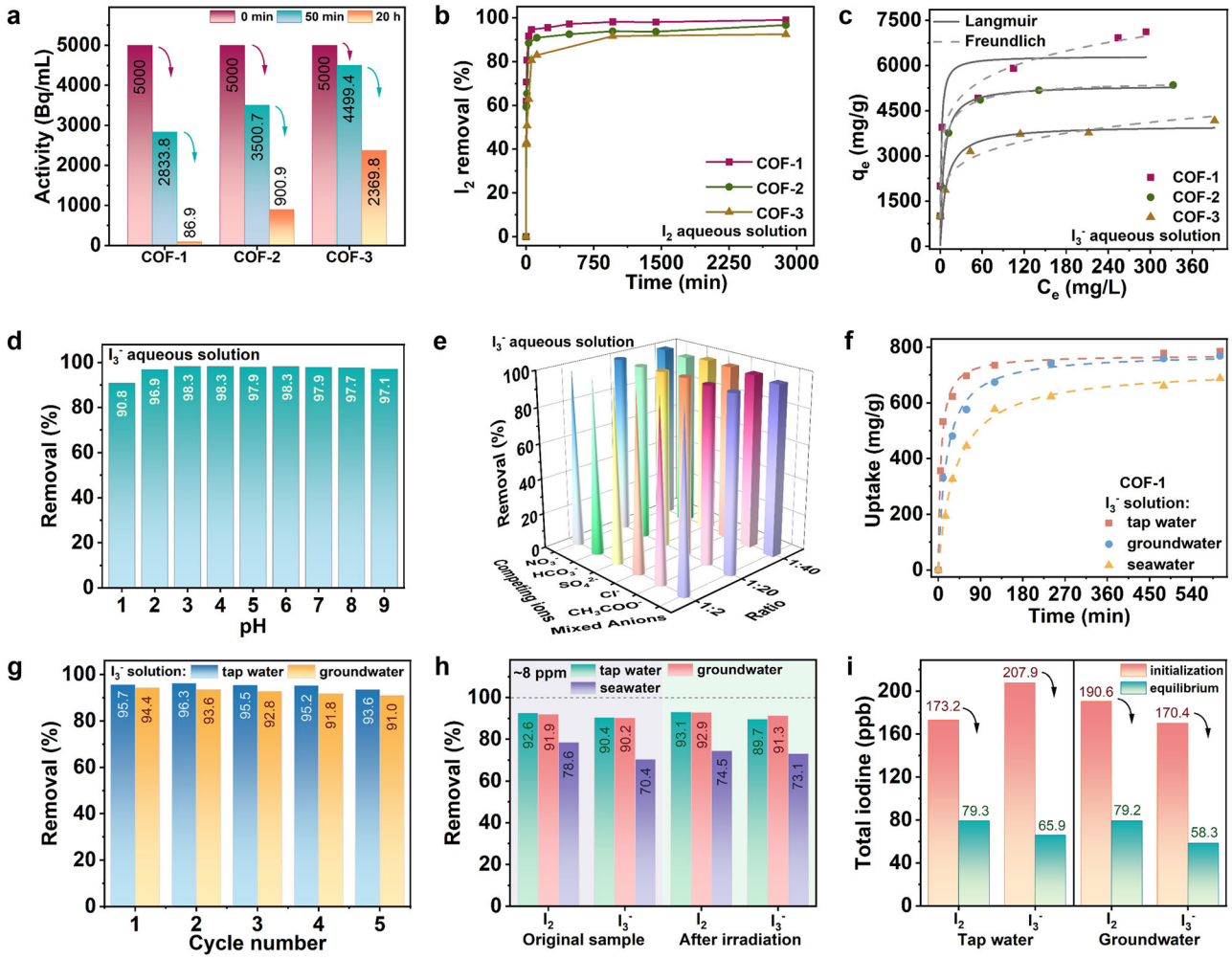


Fig. 4 | Iodine adsorption performance of COFs. a The radioactivity changes of radioactive iodine (^{131}I) in aqueous solution before and after adding COFs. **b** Static iodine adsorption on COF-1, COF-2, and COF-3 from I_2 aqueous solution. **c** Equilibrium adsorption isotherms for different COFs in KI/I_2 solution (fitted lines for the Langmuir and the Freundlich models are shown). **d** I_3^- removal from KI/I_2 solution by COF-1 over a broad pH range. **e** Selectivity of COF-1 for different anions in KI/I_2 solution. **f** I_3^- adsorption kinetics on COF-1 in iodine-spiked tap water, groundwater, and seawater (fitted lines for the pseudo-second-order kinetic model are shown). **g** Recycle test data for I_3^- removal from iodine-spiked tap water or groundwater by COF-1. **h** Removal of I_2 and I_3^- from ~8 ppm iodine-spiked tap water, groundwater, and seawater. **i** Measured total residual I_2 and I_3^- concentrations in iodine-spiked tap water and groundwater before and after adsorption on COF-1, which are presented as the average values derived from triplicate measurements. The data in (**b, c, d, f,** and **g**) present the average values obtained from three independent replicates.

environmental pollution. It is crucial to be able to efficiently remove iodine from water in emergencies. To explore the relationship between local polarity in the triangular pores of the COFs and iodine capture performance, we conducted a series of experiments to assess the capture of I_2 or I_3^- (containing ^{131}I) in water. The activity was detected using a radioactive iodine aqueous solution of ~5000 Bq/mL to mimic the radionuclide waste. After adding COF-1, COF-2, and COF-3, a significant decrease in radioactivity was observed within 50 min, with activities of 2833.8, 3500.7, and 4499.4 Bq/mL, respectively (Fig. 4a). The activities decreased to 86.9, 900.9, and 2369.8 Bq/mL after 20 h, with natural decay of ^{131}I being negligible over such a short period (Fig. 4a). Due to the scarcity of purified ^{131}I and its high radioactivity, subsequent adsorption experiments were conducted using non-radioactive iodine. Upon adding the COFs to aqueous I_2 solutions, fast I_2 uptake was seen, as inferred from UV-Vis spectroscopic studies (Fig. 4b, Supplementary Fig. 11). The adsorption data followed a pseudo-second-order kinetic model, suggesting that the rate-limiting step was a chemisorption process (Supplementary Fig. 12, Supplementary Table 5)[53]. The rate constant k_2 was found to be 1.28×10^{-3} g/mg/min for COF-1, demonstrating excellent kinetics for iodine uptake in aqueous solution. The I_2 adsorption capacities of the COFs were determined from adsorption isotherms, with uptake capabilities of 2.01, 1.79, and 1.22 g/g, respectively (Supplementary Fig. 13). The Freundlich model fitted all the adsorption curves well, suggesting a multilayer adsorption process in micropores (Supplementary Table 6)[54]. The results are explained by I_2 diffusion and adsorption at pore windows and the interlayers, resulting in effective I_2 capture by COF-1 (with I_2 adsorption being largely independent of the functional groups in the COF).

In iodine-spiked wastewater, I_2 tends to generate I_3^-, particularly in the presence of I^-, via the process of $I_2 + I^- \rightleftharpoons I_3^-$. Thus, I_3^- adsorption is also of importance to iodine remediation. The adsorption isotherms of the three COFs in KI/I_2 solution showed that I_3^- adsorption was rapid even at low concentrations, with equilibrium established following the occupation of pores. The I_3^- adsorption capacities of COF-1, COF-2, and COF-3 were 7.12, 5.35, and 4.17 g/g, respectively, indicating excellent iodine capture performance from water (Fig. 4c). Fitting to Langmuir and Freundlich models reveals that the Freundlich model provides a superior description, with higher R^2 values (Supplementary Table 7). Furthermore, UV-Vis studies showed an almost instantaneous decrease

in the I_3^- concentration upon introduction of COF-1 (Supplementary Fig. 14). The initial experiments confirmed that COF-1 possessed rapid I_3^- adsorption kinetics in 10 min, achieving an equilibrium removal of > 94.7% within 120 min, with an adsorption capacity of 236.7 mg/g (Supplementary Fig. 15, Supplementary Table 8).

Considering the challenges of iodine adsorption in practical applications, such as extreme pH, abundant competing anions, practical scenarios, and durability, we sought to explore I_2 and I_3^- capture of COF-1 from aqueous media under harsh conditions. First, extreme pH effects were evaluated. As shown in Fig. 4d, the removal efficiency for I_3^- was close to or exceeded 97% at pH ranging from 2 to 9. Notably, the I_2 and I_3^- removal efficiency of COF-1 was measured to be greater than 90% at pH 1 (Fig. 4d, Supplementary Fig. 16), indicating a strong affinity of COF-1 (possessing weak local polarity) for iodine species over a wide pH range. Motivated by the presence of possible interfering ion substances in contaminated water sources, selective I_3^- capture experiments were conducted in aqueous solutions containing an excess of possible competing anions (NO_3^-, HCO_3^-, Cl^-, SO_4^{2-}, and CH_3COO^-) (Fig. 4e). COF-1 exhibited high removal efficiencies over 99%, 98%, and 97% for I_3^-, in the presence of 2-fold, 20-fold, and 40-fold excesses of competing anions, respectively. Furthermore, the removal efficiencies were not affected by mixed anions, with the removal efficiency exceeding 95% even at high concentrations of mixed anions. COF-1 showed excellent selectivity for both forms of iodine (I_2 and I_3^-), making it a promising adsorbent for iodine recovery from polluted water environments. In tap water and groundwater, COF-1 showed removal efficiencies higher than 96% and 92%, respectively. COF-1 with weakly polar pores was found to have an excellent I_3^- uptake capability, delivering adsorption capacities of 735 mg/g within 120 min in tap water and 743 mg/g within 240 min in groundwater (Fig. 4f). The leakage of iodine into seawater, following a nuclear accident, poses a significant challenge due to the complex composition of seawater. COF-1 achieved an iodine adsorption capacity of 688 mg/g within 10 h in I_3^--spiked seawater. The fitting data followed a pseudo-second-order kinetic model, indicating that the I_3^- adsorption by COF-1 mainly involved chemical adsorption in the triangular pores and between conjugated layers (Supplementary Table 9). Durability and cycling stability are further important considerations for practical adsorbents. It is worth noting that COF-1 can be readily regenerated by elution with ethanol. The I_2 capture ability of COF-1 was almost unchanged after five adsorption-regeneration cycles (Supplementary Fig. 17). Further, COF-1 retained removal efficiencies of 93.6% and 91.0% for I_3^- after five cycles, with negligible performance losses in tap water and groundwater, respectively, suggesting its suitability for practical applications (Fig. 4g). Impressively, the I_2 and I_3^- adsorption capacities of COF-1 in water surpassed other commercial adsorbents, clearly reflecting the advantages of COFs with a weak polarity framework (Supplementary Fig. 18). Furthermore, the iodine capture performance of COF-1 surpasses or is comparable to very favorably with other state-of-the-art COFs, demonstrating the great promise for real-world applications (Supplementary Fig. 19, Supplementary Table 10).

Iodine concentrations in water are generally low in most practical scenarios. As shown in Fig. 4h, the removal efficiencies of I_2 and I_3^- were close to or exceeded 90% for tap water and groundwater (for an initial concentration of ~8 ppm). The residual I_2 and I_3^- in the spiked seawater were measured, achieving removal ratios of 78.6% for I_2 and 70.4% for I_3^-. After being subjected to irradiation treatment, COF-1 demonstrated excellent I_2 and I_3^- capture performance, achieving a similar removal efficiency to the original adsorbent in various water environments. To broaden the potential application in nuclear wastewater treatment, we also explored trace iodine capture (to mimic rapid iodine diffusion and dilution in waterways). The residual I_2 or I_3^- concentrations in aqueous solutions treated with COF-1 were 22.8 and 27.3 ppb, respectively, compared to initial concentrations of 147.2 and 177.6 ppb (Supplementary Fig. 20). Notably, the presence of a 10-fold excess of equivalent competing anions (NO_3^-, SO_4^{2-}, HCO_3^-, and Cl^-) did not impact selective iodine capture at low initial concentrations. Impressively, the residual I_2 concentration was to be 79.3 ppb in tap water, and 79.2 ppb in groundwater (for initial concentrations of ~200 ppb I_2) (Fig. 4i). Similarly, for I_3^- solutions with an initial ultra-low concentration of ~200 ppb, the residual I_3^- concentrations after treatment with COF-1 were determined to be 65.9 ppb for tap water and 58.3 ppb for groundwater.

For the treatment of radioactive iodine-spiked wastewater, tap water, groundwater, and seawater in potential industrial applications, COFs can be packed into an adsorption column in various forms (powders, granules, pellets, etc.) to capture iodine and thus minimize potential environmental impacts. As proof-of-concept, we examined the dynamic iodine adsorption performance through breakthrough experiments to evaluate the capability of COF-1. As shown in Supplementary Fig. 21, COF-1 can effectively capture I_2 from aqueous solution under slow column elution conditions, with breakthrough of I_2 occurring after ~240 min of elution. The calculated dynamic adsorption capacity at equilibrium (470 min) was 715 mg/g. For I_3^- in groundwater, COF-1 also exhibited excellent dynamic removal performance, with breakthrough of I_3^- occurring after ~200 min. These results highlight the potential of COF-1, with its weak polarity, as an iodine capture material in various water environments, positioning it as a promising solution for radioactive iodine removal.

Our findings show that regulating the polarity in triangular pores of microporous COFs can be used to enhance aqueous iodine capture. The COFs developed in this work, especially COF-1, are capable of capturing iodine from water with fast kinetics, high capacity, and good recyclability. Below, the iodine adsorption mechanism used by the COFs is investigated to explain their high adsorption efficiency.

Mechanism studies

Electrostatic potential mapping was performed to visualize the charge distribution and elucidate the polarity characteristics of the COF frameworks. COF-1 features a symmetric charge distribution, as reflected in its uniform electrostatic potential map, which lacks significant positive or negative regions, indicating a weakly polar framework (Supplementary Fig. 22). Despite this overall weak polar character, the imine-linked benzene rings undergo polarization, creating alternating regions of positive and negative electrostatic potential and thereby introducing localized polarity within the COF-1 fragment. In COF-2, both the imine and imidazole moieties act as electron-deficient centers, which amplifies the local polarity. COF-3 exhibits even more pronounced polarization, with electron-deficient sites distributed in the imine, imidazole, and phenazine units, resulting in substantially stronger polarization centers than those observed in COF-1 and COF-2. Furthermore, we conducted dielectric response measurements on compressed pellets of the COF samples (Fig. 5a). COF-1 exhibited lower dielectric constants than COF-2 and COF-3 at the same frequency, indicating weaker polarity in the COF-1 framework. The dielectric constants of COF-1 and COF-2 remained nearly unchanged with frequency, consistent with their weak polarity. In contrast, the pronounced decrease in dielectric constant of COF-3 with increasing frequency indicates relaxation polarization, implying stronger polarity. This evidence offers a compelling description of the local polarity within the COF frameworks, further reinforcing our hypothesis that COFs with weak polarity should be superior adsorbents for nonpolar I_2 and I_3^-, promoting transport of I_2/I_3^- from polar aqueous solutions onto the pore surfaces.

To explore the I_2 and I_3^- capture mechanisms used by the COFs, PXRD, FT-IR, Raman, X-ray photoelectron spectroscopy (XPS), and theoretical calculations are carried out. After I_2 capture, the sharp PXRD peaks associated with the as-prepared COFs disappeared, confirming that I_2 was bound in the pores (Supplementary Fig. 23). The adsorbed I_2 was easily released from the frameworks by ethanol

https://doi.org/10.1038/s41467-026-73328-1

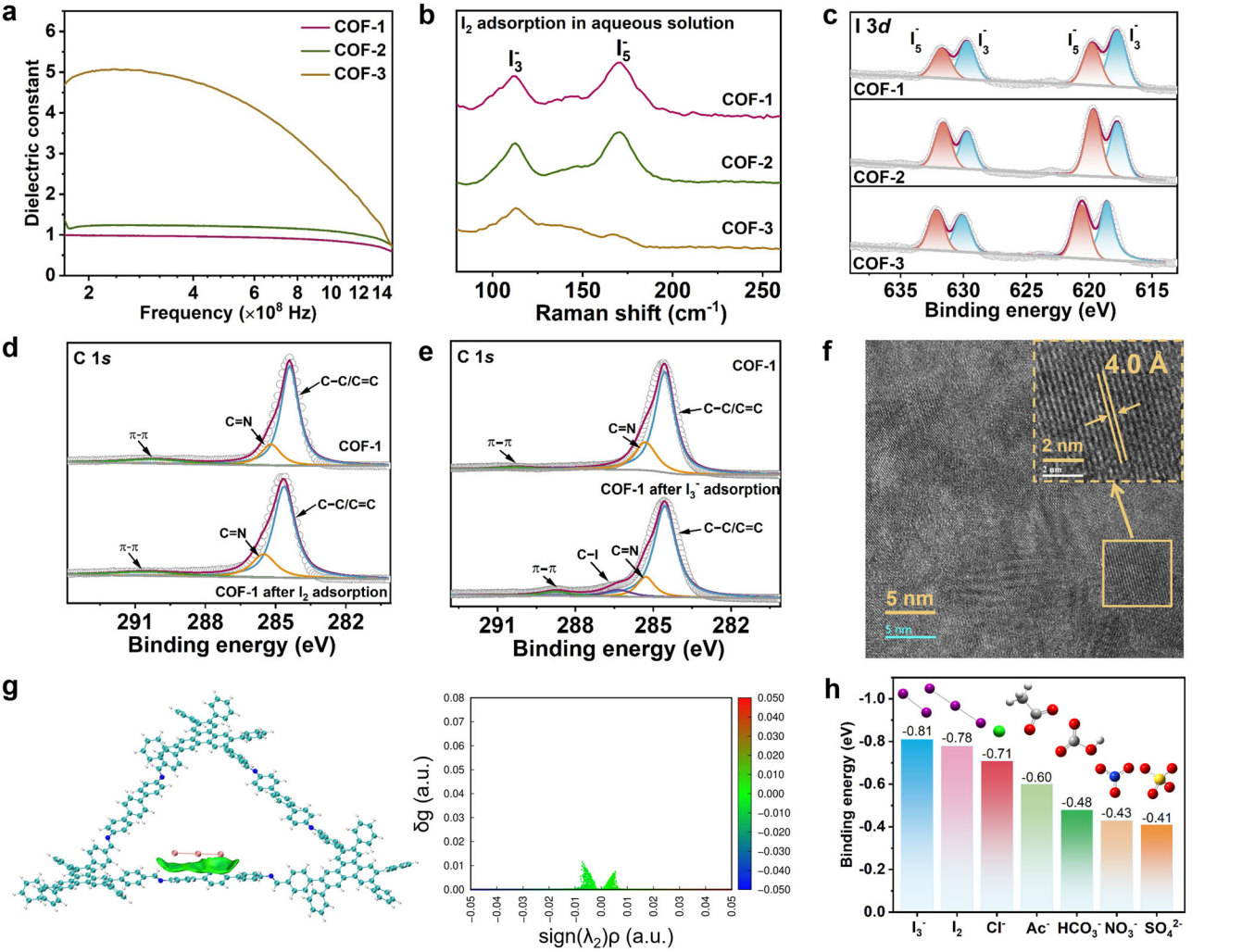


Fig. 5 | Iodine adsorption mechanisms. a Dielectric constants of COF-1, COF-2, and COF-3. **b** Raman spectra of COFs after I_2 adsorption in aqueous solution. **c** I 3*d* XPS spectra of COFs after I_2 adsorption in aqueous solution. **d** C 1*s* XPS spectra of COF-1 before and after I_2 adsorption in aqueous solution. **e** C 1*s* XPS spectra of COF-1 before and after I_3^- adsorption in KI/I_2 solution. **f** TEM image of COF-1 after I_3^- adsorption (inset: expanded view showing the lattice spacing). **g** The colored iso-surfaces corresponding to IGMH analysis of COF-1 fragment. **h** Binding free energy diagrams of I_2, I_3^- and other anions on COF-1 from DFT calculations.

treatment, resulting in the reappearance of the sharp PXRD signals of the as-prepared COFs. The PXRD data verified the excellent recyclability of the COFs (Supplementary Fig. 24). FT-IR spectra for the COFs after immersion in aqueous I_2 solutions showed the C = C stretch associated with the phenyl rings in the COFs shifted from 1603 cm^{-1} to 1599 cm^{-1} after I_2-treatment. In addition, COF-1 retains the C = N stretch, indicating that the weak polarity framework reduces the dependence of iodine adsorption on nitrogen-containing groups. Compared with COF-1, a large shift of C = N stretch was observed between as-prepared and I_2-loaded COF-2 or COF-3 (Supplementary Fig. 25)[55]. The intensities of the C − N stretching vibrations of COF-2 and COF-3 were weakened after I_2 exposure. The spectral changes suggested strong charge-transfer-induced interactions between the pores and I_2 molecules, with the N-heterocycle functionalities of imidazole and phenazine units in COF-2 and COF-3 also being involved in these interactions. After the release of I_2, the FT-IR spectra of COFs returned to their original patterns, once again proving the integrity of the COF structures (Supplementary Fig. 26). Raman spectra of I_2-loaded COFs exhibited bands at 109 and 167 cm^{-1}, associated with I_3^- and I_5^-, respectively, further indicating charge transfer from the COFs to I_2 molecules (Fig. 5b). Next, I 3*d*, C 1*s* and N 1*s* XPS data were collected for the I_2-loaded COFs, with the aim of confirming the iodine speciation and the nature of the iodine-carbon/nitrogen interactions. The I 3*d* XPS spectra for the I_2-treated COFs showed peaks of I_3^- (I $3d_{5/2}$ = 618.7 and I $3d_{3/2}$ = 630.2 eV) and I_5^- (I $3d_{5/2}$ = 620.6 and I $3d_{3/2}$ = 632.2 eV) (Fig. 5c). The C 1*s* spectrum of COF-1 showed peaks at 284.5, 285.2, and 290.2 eV, which could be assigned to C − C/C = C, C = N, and π-π* shake-up satellites, respectively (Fig. 5d)[56]. After I_2 adsorption, the corresponding peaks shifted to 284.6, 285.5, and 290.5 eV, respectively, with the small positive shifts attributed to the incorporation of I_2 in the COF interlayers by conjugation and confinement effects. The N 1*s* XPS spectrum of COF-1 showed a shift in the position of the imine-N signal from 398.7 eV to 398.9 eV after interaction with I_2 (Supplementary Fig. 27), suggesting imine-N was involved in I_2 capture. In addition, a new peak appeared at 400.5 eV related to N − I bonding, revealing the formation of charge-transfer complexes between I_2 and the heteroatom-N centers in the pores. Following COF immersion in a KI/I_2 solution, the I 3*d* peaks were observed for I_3^- (I $3d_{5/2}$ = 618.5 and I $3d_{3/2}$ = 630.2 eV) and I_5^- (I $3d_{5/2}$ = 620.6 and I $3d_{3/2}$ = 632.2 eV), suggesting the dynamic interchange of iodine species (Supplementary Fig. 28). As shown in Fig. 5e, the corresponding C 1*s* XPS spectra showed peaks for C − C/C = C, C = N at 284.6 and 285.3 eV, respectively, along with a new peak at 286.4 eV assigned to C − I, indicating the formation of charge-transfer complexes between iodine and the frameworks. The N 1*s* signals for imine C = N and N − I at 397.8 and 399.4 eV, respectively, were seen

after I_3^- capture, again indicating that the imine-N center adsorbed iodine by charge-transfer (Supplementary Fig. 29). Therefore, the synergistic effects of aromatic moieties and nitrogen-containing groups allow effective iodine adsorption. TEM image was applied to characterize the interlayer changes after adsorption, revealing the slightly widened spacing (4.0 Å) in the ordered porous structure, consistent with interlayer adsorption of I_2 or I_3^- (Fig. 5f). This provided direct evidence of interlayer expansion within the ordered porous structure from 3.6 Å to 4.0 Å. To elucidate the nature of the interactions between the COF framework and I_3^-, an Independent Gradient Model based on Hirshfeld partition (IGMH) analysis was performed (Fig. 5g). The IGMH isosurface maps show distinct green regions localized between the benzene rings of the COF and the I_3^- anion. The sign(λ_2)ρ values in these regions fall within the range typical for van der Waals interactions, which play a significant role in the adsorption process. The absence of red isosurfaces in the IGMH plots confirms that the interaction is free from significant spatial constraints. Zeta potential measurements showed that COF-1 exhibited negative zeta potentials from pH ~3.8 to 7.0 (Supplementary Fig. 30). For COF-2 and COF-3, the zeta potentials only became negative at pH values > 5. The charged frameworks were expected to be beneficial for the I_2 approach to frameworks. Therefore, these observations indicate that van der Waals forces and charge-transfer are facilitated by both the pore channels and interlayer spaces of the triangular weak-polarity framework.

We next carried out binding energy calculations to better understand the I_2 and I_3^- adsorption mechanisms on the COF-1 (Fig. 5h and Supplementary Fig. 31). The binding free energies of fragments with I_2 or I_3^- were -0.78 and -0.81 eV, respectively, suggesting a strong affinity between I_2 or I_3^- and triangular pore structures with weak polarity. In contrast, competing anions such as Cl^-, NO_3^-, HCO_3^-, CH_3COO^- and SO_4^{2-}, are either more hydrophilic or possess structural polarity, and are captured via ion exchange or electrostatic adsorption. The neutral, hydrophobic surfaces of COF-1 lack the corresponding sites, rendering these anions incapable of adsorption. The binding energies between the COF-1 framework and iodine (I_2 and I_3^-) significantly exceed those calculated for other anions, including Cl^- (-0.71 eV), NO_3^- (-0.43 eV), HCO_3^- (-0.48 eV), SO_4^{2-} (-0.41 eV), and CH_3COO^- (-0.60 eV). These findings demonstrate that the weakly polar COF-1 serves as an effective platform for selectively binding I_2 and I_3^-, offering promising potential for applications requiring iodine capture in the presence of competing anions.

The above results demonstrate that COF-1 with triangular channels could bond with iodine through imine groups and the carbon framework by charge transfer, whilst accommodating I_2 and I_3^- in the pores driven by hydrophobic interactions and van der Waals forces, collectively promoting efficient I_2 and I_3^- adsorption in water. The weakly polar framework of COF-1 reduced interference from water molecules on structurally nonpolar I_2 and I_3^- uptake, weakening the dependence on functional groups that provide transferable electrons. The 1D micropores offer near-ideal spatially independent nanospaces that do not interfere with one another, resulting in high total iodine removal performance. The mechanistic insights provided by this work guide the design of high-performance adsorbents for iodine capture.

Discussion

Concerns about the hazards of radioactive iodine motivate the search for efficient iodine capture materials from water. To address potential applications in processing radioactive iodine-spiked wastewater, groundwater, tap water, and seawater, COF-based adsorbents were developed herein for selective iodine capture from these water sources. This work is of great significance for the sustainable development of nuclear energy and environmental remediation. Specifically, we investigated local polarity regulation in COFs with triangular micropores. The triangular pores promote the diffusion and adsorption of structurally nonpolar I_2 and I_3^-, while the weakly polar pores in COF-1 avoid competitive adsorption of H_2O molecules or other ions. The frameworks induced strong interactions with I_2 and I_3^- by hydrophobic interaction, charge transfer, π-conjugation and van der Waals forces. The developed COF-1 adsorbent exhibited fast adsorption kinetics for I_2 and I_3^-, high adsorption capacities, pH adaptability, selectivity, and good reusability under a wide range of conditions. Specifically, COF-1 demonstrates high iodine adsorption capacities (2.01 g/g in an I_2 solution and 7.12 g/g in KI/I_2 solution) and fast adsorption kinetics, removing over 90% of iodine within 30 min. Moreover, COF-1 can capture I_2 or I_3^- from contaminated tap water, groundwater, and seawater, even in the presence of large excesses of competing anions, whilst also demonstrating efficient ^{131}I removal from water at low (trace) concentrations. COF-1 is a state-of-the-art iodine adsorbent under both static adsorption conditions and dynamic adsorption conditions. Taken together, this work guides the development of improved COF-based sorbents for iodine pollutants that not only rely solely on polar functional groups (such as nitrogen-containing groups) but also utilize weak pore polarity for environmental remediation, water purification, and other applications.

Methods

Synthesis of COF-1

In a 5 mL glass tube, 4,4′,4″,4‴,4⁗,4⁗′-(triphenylene-2,3,6,7,10,11-hexayl)hexabenzaldehyde (HFPTP, 8.53 mg) and 4,4″-diamino-p-terphenyl (DPT, 7.8 mg) were dissolved in a solvent mixture of mesitylene (Mes, 0.3 mL)/1,4-dioxane (Dox, 0.6 mL)/acetic acid (6 M AcOH, 0.1 mL). The mixture was then frozen in a liquid nitrogen bath, then sealed with a gas torch. After being heated at 120 °C for 72 h, the COF-1 product was washed several times with tetrahydrofuran, acetone, and n-hexane, before being collected by filtration and finally dried under vacuum overnight.

Synthesis of COF-2

In a 5 mL glass tube, HFPTP (8.53 mg) and 4,4′-(1H-benzo[d]imidazole-4,7-diyl)dianiline (DBID, 9 mg) were dissolved in the solution of Mes (0.6 mL), Dox (0.3 mL) and 6 M AcOH (0.09 mL). The mixture was then frozen in a liquid nitrogen bath and sealed with a gas torch. After being heated at 120 °C for 72 h, the COF-2 product was washed several times with tetrahydrofuran, acetone, and n-hexane, before being collected by filtration and finally dried under vacuum overnight.

Synthesis of COF-3

In a 5 mL glass tube, 2,3,8,9,14,15-hexa(4-formylphenyl)diquinoxalino[2,3-a:2′,3′-c]phenazine (HATN, 10.1 mg) and DBID (9 mg) were dissolved in a solvent mixture of N,N-dimethylacetamide (DMA, 0.8 mL), o-dichlorobenzene (o-DCB, 0.2 mL) and 6 M AcOH (0.08 mL). The mixture was then frozen in a liquid nitrogen bath, then sealed with a gas torch. After being heated at 120 °C for 72 h, the COF-3 product was washed several times with tetrahydrofuran, acetone, and n-hexane, before being collected by filtration and finally dried under vacuum overnight.

Radioactive iodine adsorption

All operations relating to the handling of ^{131}I were performed in a licensed radiochemical laboratory. Radioactive iodine molecules ($^{131}I_2$) were injected into the I_2/KI solution of ~8 ppm to ensure that radioactive iodine was not easily volatilized. The initial activity of ^{131}I is detected. Adsorption experiments were carried out at a fixed adsorbent/liquid ratio of 2 mg/mL. COFs were dispersed in a solution (2 mL) containing ^{131}I at a specific activity. Aliquots were collected at regular time intervals while constantly stirring the dispersion. The adsorbents were collected on a 0.22 μm membrane filter, and radioactive iodine in the filtrate was quantified using a liquid scintillation counting (LSC) system.

I_2 or I_3^- adsorption kinetics studies

The adsorption kinetics experiments for the different COFs were carried out in aqueous solution containing ~100 ppm I_2 or ~50 ppm I^-/I_2 at a fixed adsorbent/liquid ratio of 0.2 g/L. Aliquots were collected at regular time intervals while the dispersion was constantly shaken. The dispersions were filtered on a 0.22 μm membrane filter and the filtrate examined by UV-Vis spectroscopy over the range of 200–600 nm.

The iodine removal efficiency (%) of the COFs was determined using the following equation:

$$R(\%) = \frac{C_0 - C_t}{C_0} \times 100\% \quad (1)$$

where C_O (mg/L) and C_t (mg/L) are the concentrations of I_2 or I_3^- before and after adsorption, respectively. The amount of adsorbed I_2 or I_3^- was determined using the following equation:

$$q_t = \frac{(C_0 - C_t) \times V}{m} \quad (2)$$

where q_t (mg/g) is the amount of I_2 or I_3^- adsorbed per gram of adsorbent at time t (min), C_O (mg/L) and C_t (mg/L) are the initial and residual concentrations of I_2 or I_3^- in the stock solution and filtrate, respectively, and m (g) is the mass of adsorbent used in the study.

Adsorption capacity studies

The I_2 adsorption capacity experiments in water were carried out at 25 °C. COFs were added into aqueous solutions with I_2 concentrations ranging from ~10 to ~200 ppm at a fixed adsorbent/liquid ratio of 0.05 g/L. The dispersions were shaken for 48 h and then filtered on a 0.22 μm membrane filter to remove the adsorbents. After filtration, the I_2 concentrations in the filtrate were determined by UV-Vis spectroscopy at 200–600 nm. Similarly, COFs were added into KI/I_2 aqueous solutions with iodine concentrations ranging from ~50 to ~650 ppm at a fixed adsorbent/liquid ratio of 0.05 g/L. The dispersions were shaken for 24 h and then filtered on a 0.22 μm membrane filter to remove the adsorbents. After filtration, the I_3^- concentrations in the filtrate were determined by UV-Vis spectroscopy at 200-550 nm.

Selectivity of I_3^- capture

The effect of possible competing anions on I_3^- adsorption by COF-1 was studied by adding NO_3^-, HCO_3^-, Cl^-, CH_3COO^-, or SO_4^{2-} (~100, 1000 or 2000 ppm) into an I^-/I_2 solution of 50 ppm. COF-1 (2.0 mg) was added to 10 mL of I^-/I_2 solutions containing NO_3^-, HCO_3^-, Cl^-, CH_3COO^-, or SO_4^{2-}, respectively. After shaking for 48 h, the adsorbent was removed on a 0.22 μm membrane filter, and residual triiodide concentrations quantified by UV-Vis spectroscopy.

Data availability

The authors declare that all the data supporting the findings of this study are available within the article (and Supplementary Information Files), or additional data are available from the corresponding author upon request. Source data https://doi.org/10.6084/m9.figshare.31931712 are provided within this paper.

References

1. Chu, S. & Majumdar, A. Opportunities and challenges for a sustainable energy future. *Nature* **488**, 294–303 (2012).
2. Jia, T., Shi, K., Wang, Y., Yang, J. & Hou, X. Sequential separation of iodine species in nitric acid media for speciation analysis of ^{129}I in a PUREX process of spent nuclear fuel reprocessing. *Anal. Chem.* **94**, 10959–10966 (2022).
3. Gilbert, A. Q. & Bazilian, M. D. Can distributed nuclear power address energy resilience and energy poverty? *Joule* **4**, 1839–1843 (2020).
4. Ma, Y. et al. Porous aromatic framework with multifunctional sites for effective recovery of various trace iodine species from water. *Adv. Sci.* **12**, 2500993 (2025).
5. Wang, P. et al. Exceptional iodine capture in 2D covalent organic frameworks. *Adv. Mater.* **30**, 1801991 (2018).
6. Liu, J. et al. The transport, distribution, and budget of anthropogenic ^{129}I in the Bohai and North Yellow Seas, China. *J. Hazard. Mater.* **487**, 137101 (2025).
7. Fan, Y. et al. Pathways of south-derived iodine-129 intrusion into Tibet as revealed by its spatial distribution. *J. Hazard. Mater.* **489**, 137570 (2025).
8. Liu, Y. et al. Reconstruction of the sources and their contributions to ^{129}I in northern Xinjiang, China. *Environ. Sci. Technol.* **57**, 10070–10078 (2023).
9. Xu, C. et al. Radioiodine sorption/desorption and speciation transformation by subsurface sediments from the Hanford site. *J. Environ. Radioact.* **139**, 43–55 (2015).
10. Riley, B. J. et al. Chalcogen-based aerogels as sorbents for radionuclide remediation. *Environ. Sci. Technol.* **47**, 7540–7547 (2013).
11. Tai, B. et al. Flexible interdigitated layered framework with multiple accessible active sites for high-performance CH_3I capture. *Sci. China Chem.* **67**, 1569–1577 (2024).
12. Wang, X.-S. et al. Occurrence of iodophenols in aquatic environments and the deiodination of organic iodine with ferrate (VI). *Environ. Sci. Technol.* **56**, 16104–16114 (2022).
13. Hao, M. et al. Advanced porous adsorbents for radionuclides elimination. *EnergyChem* **5**, 100101 (2023).
14. Buesseler, K. O. Opening the floodgates at Fukushima. *Science* **369**, 621–622 (2020).
15. Guo, J., Xiong, H., Liu, H., Zhang, T. & Sun, X. Radioiodine based biomedical carriers for cancer theranostics. *Coord. Chem. Rev.* **497**, 215430 (2023).
16. Ma, R. et al. Deficiency and excess of groundwater iodine and their health associations. *Nat. Commun.* **13**, 7354 (2022).
17. Smith, J. P., Oktay, S. D., Kada, J. & Olsen, C. R. Iodine-131: a potential short-lived, wastewater-specific particle tracer in an urbanized estuarine system. *Environ. Sci. Technol.* **42**, 5435–5440 (2008).
18. Riley, B. J., Vienna, J. D., Strachan, D. M., McCloy, J. S. & Jerden, J. L. Materials and processes for the effective capture and immobilization of radioiodine: a review. *J. Nucl. Mater.* **470**, 307–326 (2016).
19. Pan, T., Yang, K., Dong, X. & Han, Y. Adsorption-based capture of iodine and organic iodides: status and challenges. *J. Mater. Chem. A* **11**, 5460–5475 (2023).
20. Mishra, B. et al. Diketopyrrolopyrrole-based donor–acceptor covalent organic frameworks for iodine capture. *Small* **21**, 2411199 (2025).
21. Li, X. et al. Moderate and universal synthesis of undoped covalent organic framework aerogels for enhanced iodine uptake. *Chem. Mater.* **34**, 11062–11071 (2022).
22. Shui, F. et al. Iodine nanotrap for highly efficient iodine capture under high temperature. *Chem. Eng. J.* **468**, 143525 (2023).
23. O'Shaughnessy, M. et al. Porous isoreticular non-metal organic frameworks. *Nature* **630**, 102–108 (2024).
24. Zhao, Q. et al. In situ confined synthesis of a copper-encapsulated silicalite-1 zeolite for highly efficient iodine capture. *Inorg. Chem.* **61**, 20133–20143 (2022).
25. Zheng, Z. et al. Recent advances in iodine adsorption from water. *Coord. Chem. Rev.* **511**, 215860 (2024).
26. Zhou, W. et al. Nonporous amorphous superadsorbents for highly effective and selective adsorption of iodine in water. *Nat. Commun.* **14**, 5388 (2023).
27. Wang, H.-Z., Chan, M. H.-Y. & Yam, V. W.-W. Heavy-metal ions removal and iodine capture by terpyridine covalent organic frameworks. *Small Methods* **8**, 2400465 (2024).

28. Chapman, K. W., Chupas, P. J. & Nenoff, T. M. Radioactive iodine capture in silver-containing mordenites through nanoscale silver iodide formation. *J. Am. Chem. Soc.* **132**, 8897–8899 (2010).
29. Pham, T. C. T. et al. Capture of iodine and organic iodides using silica zeolites and the semiconductor behaviour of iodine in a silica zeolite. *Energy Environ. Sci.* **9**, 1050–1062 (2016).
30. Zhang, X. et al. Mechanically interlocked aerogels with densely rotaxanated backbones. *J. Am. Chem. Soc.* **144**, 11434–11443 (2022).
31. Zheng, B., Lin, X., Zhang, X., Wu, D. & Matyjaszewski, K. Emerging functional porous polymeric and carbonaceous materials for environmental treatment and energy storage. *Adv. Funct. Mater.* **30**, 1907006 (2020).
32. Jeong, H. et al. Selective removal of radioactive iodine from water using reusable Fe@Pt adsorbents. *Water Res* **222**, 118864 (2022).
33. Xie, L. et al. Calix[4]pyrrole-based crosslinked polymer networks for highly effective iodine adsorption from water. *Angew. Chem. Int. Ed.* **61**, e202113724 (2022).
34. Zhang, Y. et al. Superior iodine uptake capacity enabled by an open metal-sulfide framework composed of three types of active sites. *CCS Chem.* **5**, 1540–1548 (2023).
35. Zhang, Q. & Luo, F. Fabricating boron-functionalized covalent organic framework with remarkable potential in handling cationic, anionic, and gaseous nuclear wastes. *Adv. Funct. Mater.* **34**, 2401775 (2024).
36. Cao, X. et al. A tetraaldehyde-derived porous organic cage and covalent organic frameworks: Syntheses, structures, and iodine vapor capture. *Chin. Chem. Lett.* **35**, 109201 (2024).
37. Liu, X. et al. Porous organic cage as an efficient platform for industrial radioactive iodine capture. *Angew. Chem. Int. Ed.* **63**, e202411342 (2024).
38. Dai, D. et al. Macrocyclic arenes-based conjugated macrocycle polymers for highly selective CO_2 capture and iodine adsorption. *Angew. Chem. Int. Ed.* **60**, 8967–8975 (2021).
39. Chen, D. et al. Multi-functionalization integration into the electrospun nanofibers exhibiting effective iodine capture from water. *ACS Appl. Mater. Interfaces* **14**, 47126–47135 (2022).
40. Fajal, S. et al. Ultralight crystalline hybrid composite material for highly efficient sequestration of radioiodine. *Nat. Commun.* **15**, 1278 (2024).
41. Jiang, S.-Y. et al. Creating amphiphilic porosity in two-dimensional covalent organic frameworks via steric-hindrance-mediated precision hydrophilic-hydrophobic microphase separation. *Nat. Commun.* **15**, 698 (2024).
42. He, T. & Zhao, Y. Covalent organic frameworks for energy conversion in photocatalysis. *Angew. Chem. Int. Ed.* **62**, e202303086 (2023).
43. Zhou, Z. et al. Carbon dioxide capture from open air using covalent organic frameworks. *Nature* **635**, 96–101 (2024).
44. Li, Y., Chen, W., Xing, G., Jiang, D. & Chen, L. New synthetic strategies toward covalent organic frameworks. *Chem. Soc. Rev.* **49**, 2852–2868 (2020).
45. Liu, R. et al. Linkage-engineered donor–acceptor covalent organic frameworks for optimal photosynthesis of hydrogen peroxide from water and air. *Nat. Catal.* **7**, 195–206 (2024).
46. Wang, P. et al. High-precision size recognition and separation in synthetic 1D nanochannels. *Angew. Chem. Int. Ed.* **58**, 15922–15927 (2019).
47. Li, Z. et al. Electronegative strategic positions in covalent organic frameworks: unlocking high-efficiency gold recovery. *Angew. Chem. Int. Ed.* **64**, e202502199 (2025).
48. Xu, S. et al. A nitrogen-rich 2D sp^2-carbon-linked conjugated polymer framework as a high-performance cathode for lithium-ion batteries. *Angew. Chem. Int. Ed.* **58**, 849–853 (2019).
49. Lin, Y. et al. An elastic hydrogen-bonded cross-linked organic framework for effective iodine capture in water. *J. Am. Chem. Soc.* **139**, 7172–7175 (2017).
50. Ma, Y. et al. Local charge density enhancement strategy in nitrogen-rich covalent organic framework for boosted iodine removal from water. *Adv. Sci.* **12**, e00697 (2025).
51. Liu, Y. et al. Enhanced hydrogen peroxide photosynthesis in covalent organic frameworks through induced asymmetric electron distribution. *Nat. Synth.* **4**, 134–141 (2025).
52. Lan, X. et al. Covalent organic framework with donor^1-acceptor-donor^2 motifs regulating local charge of intercalated single cobalt sites for photocatalytic CO_2 reduction to syngas. *Angew. Chem. Int. Ed.* **63**, e202407092 (2024).
53. Arora, N. et al. Rapid, high-capacity adsorption of iodine from aqueous environments with amide functionalized covalent organic frameworks. *Chem. Sci.* **15**, 3571–3577 (2024).
54. Chen, R., Hu, T. & Li, Y. Stable nitrogen-containing covalent organic framework as porous adsorbent for effective iodine capture from water. *React. Funct. Polym.* **159**, 104806 (2021).
55. Hao, M. et al. Pore space partition synthetic strategy in imine-linked multivariate covalent organic frameworks. *J. Am. Chem. Soc.* **146**, 1904–1913 (2024).
56. Mei, Z. Y. et al. Regulated high-spin state and constrained charge behavior of active cobalt sites in covalent organic frameworks for promoting electrocatalytic oxygen reduction. *Angew. Chem. Int. Ed.* **62**, e202303871 (2023).

Author contributions

All authors have given approval to the final version of the manuscript. H.Y., X.W. and S.M. conceived and designed the research. M.H., Y.W., J.Z., and X.Z. performed the synthesis and characterization and conducted the experiments. M.H., X.L., and J.L. conducted the radioactive iodine (containing ^{131}I) adsorption experiments. M.H., M.L., X.Z., Z.C., G.I.N.W., A.M.A-E., A.N., and H.Y. participated in discussions. M.H. and X.Z. repeated experiments. M.H. performed the DFT calculations. M.H., H.Y., X.W, G.I.N.W., and S.M. wrote the manuscript.

Funding

This work was supported by the National Science Foundation of China (Grants 22322603, H.Y.; 22506048, M.H.; 12441508, J.L.; 22341602, Z.C.; U24B20195, X.W.); the Beijing Outstanding Young Scientist Program (X.W.); the Fundamental Research Funds for the Central Universities (2025MS052, M. H.). Partial support from the MacDiarmid Institute for Advanced Materials and Nanotechnology (G.I.N.W.). Partial support from the Robert A Welch Foundation (B-0027, S.M.) and the Ongoing Research Funding Program (ORF-2026-79), King Saud University, Riyadh, Saudi Arabia (A.N.) is also acknowledged.

Competing interests

The authors declare no competing interests.

Additional information

Supplementary information The online version contains supplementary material available at https://doi.org/10.1038/s41467-026-73328-1.

Correspondence and requests for materials should be addressed to Hui Yang, Shengqian Ma or Xiangke Wang.

Peer review information *Nature Communications* thanks Pei-Zhou Li and the other, anonymous, reviewer for their contribution to the peer review of this work. A peer review file is available.

Reprints and permissions information is available at http://www.nature.com/reprints

Publisher's note Springer Nature remains neutral with regard to jurisdictional claims in published maps and institutional affiliations.

Open Access This article is licensed under a Creative Commons Attribution-NonCommercial-NoDerivatives 4.0 International License, which permits any non-commercial use, sharing, distribution and reproduction in any medium or format, as long as you give appropriate credit to the original author(s) and the source, provide a link to the Creative Commons licence, and indicate if you modified the licensed material. You do not have permission under this licence to share adapted material derived from this article or parts of it. The images or other third party material in this article are included in the article's Creative Commons licence, unless indicated otherwise in a credit line to the material. If material is not included in the article's Creative Commons licence and your intended use is not permitted by statutory regulation or exceeds the permitted use, you will need to obtain permission directly from the copyright holder. To view a copy of this licence, visit http://creativecommons.org/licenses/by-nc-nd/4.0/.

© The Author(s) 2026